

# Model Experiments for Explaining the Processes Occurring During Conductive Battery Electrode Drying

Christiane Zihrl,\* Silas Wolf, and Arno Kwade

During the manufacturing of lithium-ion-battery electrodes, the drying step has a great impact on their performance as it determines the pore microstructure and the mechanical integrity of the electrode. To derive dependencies of the electrode properties on the drying temperature, water-based graphite anodes are dried by means of a conductive drying apparatus and analyzed during and after the drying process. Drying experiments with different temperatures from 40 to 80 °C indicate that the electrode properties strongly depend on the chosen temperature and, therefore, on the drying rate, as the investigation of the binder distribution shows. Higher drying temperatures lead to a poorly distributed binder profile with the accumulation of binder toward the surface of the coating, due to the fast receding film surface. Also, lower temperatures hinder the diffusion of the binder during the process, which also results in a less distributed binder concentration. On the contrary, the drying rate does not seem to have a major effect on the pore structure of the electrode which suggests that the binder distribution does not play a leading role in the pore structure formation process.

## 1. Introduction

Even though being introduced in 1991, lithium-ion batteries are still under intensive research due to their high potential as long-lasting, fast-charging power sources. To fulfill the needs of the upcoming electrification of transportation, many improvements have been made in the last few years.<sup>[1]</sup> One of the major influences on the later cell performance can be found in the microstructure of the electrodes.<sup>[2]</sup> It defines the ability of lithium ions to diffuse into the network and therefore, to react with

the applied active material, with larger porosity allowing the ions to diffuse more easily.<sup>[3]</sup> Contrary to that, the electrical conductivity is promoted by high interconnectivity of active material particles and conductive additives so those two counteracting influences have to be carefully evaluated for optimizing not only the cell's energy density but also its (dis)charge capability during cycling.<sup>[4,5]</sup> Apart from the microstructure, the mechanical integrity of the electrode needs to fulfill certain requirements by upholding the contact between the particles and also between the particles and the current collector, which ultimately impacts the cell performance as well.

During manufacturing, lithium-ion battery electrodes undergo a series of process steps that define the electrode's microstructure.<sup>[1,2,5]</sup> The process steps that have been


subject to intensive research, such as the dry mixing of the components,<sup>[6,7]</sup> the dispersing of the active and additive materials in the solvent,<sup>[8,9]</sup> the coating of the current collector foil with the resulting slurry,<sup>[10,11]</sup> the drying of the coated film<sup>[12–17]</sup> and the calendaring,<sup>[18–21]</sup> where the microstructure is compressed.

While all of these processes have a certain influence on the electrode structure, in general, the particle arrangement is fixed during the drying step. This means, the drying step defines the electrode pore structure, which can afterward be further compressed by calendaring. Also, the drying process has a large impact on the mechanical integrity of the electrode by influencing the binder distribution within the electrode due to accumulation at the drying front, therefore limiting the cohesive and adhesive strength of the electrode. Electrical conductivity, in contrast, is affected by the distribution of the conductive additive, which is also prone to migration, and contact with the active material. These complex processes occurring during the drying process on the microscale are not fully elucidated yet and, therefore, leave room for optimizing the overall battery performance.

The effect of drying conditions on microstructure, additive distribution, and the resulting cell performance has been examined in some studies. Hagiwara et al. examined the binder distribution during the drying of water-based anodes by measuring the migration of styrene butadiene rubber (SBR) by means of freeze-drying the anodes and analyzing the binder distribution with Raman spectroscopy. Here, a migration of the binder for temperatures of 150 °C could be detected.<sup>[22]</sup> Westphal et al. investigated the influence of convective drying parameters such as temperature and nozzle speed on electrode adhesion,

C. Zihrl, S. Wolf, A. Kwade  
Institute for Particle Technology  
Technische Universität Braunschweig  
Volkmaroder Str. 5, 38104 Braunschweig, Germany  
E-mail: a.kwade@tu-braunschweig.de

C. Zihrl, S. Wolf, A. Kwade  
Battery LabFactory Braunschweig  
Technische Universität Braunschweig  
Langer Kamp 8, 38106 Braunschweig, Germany

 The ORCID identification number(s) for the author(s) of this article can be found under <https://doi.org/10.1002/ente.202200671>.

© 2023 The Authors. Energy Technology published by Wiley-VCH GmbH. This is an open access article under the terms of the Creative Commons Attribution-NonCommercial-NoDerivs License, which permits use and distribution in any medium, provided the original work is properly cited, the use is non-commercial and no modifications or adaptations are made.

DOI: 10.1002/ente.202200671

elasticity, and conductivity and correlated these with the separation of the binder during the electrode drying, with fewer migration occurring when the diffusional binder remixing is able to outperform the evaporation driving force.<sup>[15]</sup> In a subsequent study, critical values for the driving force and the mass loading to avoid additive segregation could be determined.<sup>[16]</sup> Structure formation and binder segregation were also thoroughly explored in a series of studies conducted by Jaiser et al. In the first study, they proposed a top-down consolidation front of graphite particles responsible for binder segregation during the drying of anodes.<sup>[14]</sup> This theory has been revised in the following publication, where cryo-focused ion-beam (FIB)-secondary electron microscope (SEM) and energy-dispersive X-ray spectroscopy has been applied to examine the electrode microstructure at various points in time.<sup>[23]</sup> The particles have been found to be distributed equally every time and the pore emptying after consolidation has been proven to be heterogeneous, as also mentioned in another publication, where pore emptying has been examined by means of fluorescence emission.<sup>[24]</sup> Binder migration has been observed as well, however, no final clarification of the causative mechanisms could be presented.<sup>[23]</sup> These findings have ultimately been used to develop a three-stage drying profile, leading to adhesive electrode strengths similar to that of electrodes dried with low drying rates with the advantage of a significant drying time reduction.<sup>[13]</sup>

Apart from experimental examination, numerical modeling can be useful to gain insight into the processes, leading to different results during drying without the effort and costs of experimental investigations. Liu and Mukherjee developed a mesoscale kinetic Monte Carlo model in 2014 for evaluating the influence of particle morphology and solvent evaporation dynamics on the distribution of the different phases (active material, conductive additive, binder) after drying with a focus on structural properties rather than evaluating the binder migration.<sup>[25]</sup> This approach was subsequently extended to account for different mixing conditions<sup>[26]</sup> and various binder lengths.<sup>[27]</sup> An approach by Forouzan et al. used coarse-grained molecular dynamics for modeling the active materials together with the carbon binder domain (CBD), using shrinking CBD particles mimicking the drying process to describe effects on the final microstructure.<sup>[28]</sup> This concept was recently adapted by Ngandjong et al. and Rucci et al. for use in a multiscale simulation platform linking electrode processing with cell performance.<sup>[29,30]</sup> Additional to experimental studies, Stein et al. modeled the redistribution of secondary particles (conductive additive + binder) after the consolidation of active material particles by means of volume fractions subjected to film shrinkage which lead to different degrees of migration depending on the Peclet number.<sup>[17]</sup> Font et al. focused their modeling approach on the evolution of the binder distribution by solving an advection-diffusion equation dependent on the liquid and solid (active material) volume fractions calculated via a separate transport model.<sup>[31]</sup>

In this work, the drying of water-based anodes is examined using a model setup, in which the drying progress can be examined in real time by means of laser triangulation measurements. The extracted information about receding surface speed, drying rate, and film temperature is correlated with the microstructure development, represented by porosity and pore size distribution, as well as the binder distribution. The resulting observations lead to conclusions about the interplay between drying rate, structure

formation, and binder diffusion and show the utilizability of the presented model dryer for a defined examination of drying processes with special attention to the potential use in combination with a numerical model.

Electrode drying on an industrial scale does not allow any process variations in the sense of research due to the required material quantities as well as the inline analytics and the respective corresponding costs, so experiments on a model scale or pilot scale have to be resorted to. The latter was carried out, for example, by Westphal et al.,<sup>[15,16]</sup> where the drying process itself is largely seen as a black box and the focus was on downstream structural differences. However, model experiments such as those carried out here or by Jaiser et al.<sup>[13,14]</sup> provide a deep insight into the process during drying. Insights gained here sharpen the picture and allow for a second step a transfer to the industrial process and targeted process adaptations to improve the electrode quality influenced by drying. The results also provide important data for simulating binder distribution during drying. This test setup allows the conclusion to be drawn from the decrease in coating thickness, solids content, and coating temperature. While in industrial dryers at best the surface temperature can be determined with infrared sensors, the continuous recording of the coating thickness and the determination of the solids content is not possible. It, therefore, makes sense to present and discuss these correlations in this model test, which then allows conclusions to be drawn with the more limited possibilities of industrial dryers.

## 2. Results and Discussion

In the following, the results determined in the drying test rig for drying of a water-based anode suspension with an initial solvent content of 52% are discussed. On the basis of these results, basic findings on binder distribution and pore structure of the investigated anodes are shown and discussed.

### 2.1. Evolution of Film Properties during Drying

During the electrode drying process, the coating film is formed, which is accompanied by a decrease in the thickness of the electrode coating  $\delta_B$ . During the reduction of the coating thickness, the coating components can be rearranged, thus also causing the migration of the binder to the coating surface. By measuring the decrease in coating thickness, the segregation phenomena of the binder can be correlated with the rate of decrease in coating thickness. **Figure 1** shows the change in the layer thickness of the electrode coating  $\delta_B$  over the drying time. For the anode dried at  $T_{Dr} = 70^\circ\text{C}$ , the layer thickness decrease takes place within the first 82 s at a constant rate of decrease, resulting in a linear course in this first section. After 82 s, the reduction of the layer thickness is completed, thus the volume is fixed at this point in time. Further mass transfer processes can now only take place within this volume. After the time of volume fixation, which is further referred to as the end of shrinkage ( $t_{EoS}$ ), the layer thickness remains constant and the rate of shrinkage  $\psi$  is zero. The change in coating thickness between the linear decrease and the remaining of the coating at a constant level is characterized by a very small transition area, in which the value decreases and finally reaches  $0\text{ }\mu\text{m s}^{-1}$ . Due to the low specificity, this area is neglected

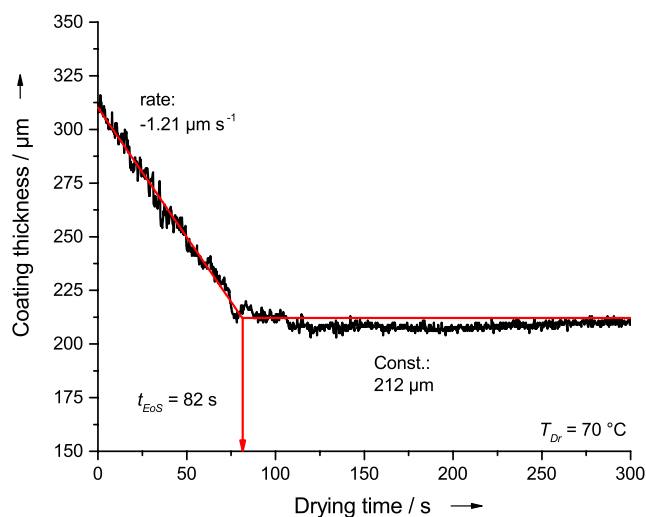


**Figure 1.** Evolution of coating thickness over time at  $T_{Dr} = 70\text{ }^{\circ}\text{C}$ .

for further consideration, so a direct transition of the linear decrease to a constant film thickness is assumed as simplification. For the comparison of  $\psi$  at different drying settings, the value range of the linear decrease is fitted. For the determination of  $\psi$ , this linear range is stretched until the mean value of  $\psi$  for the next 50 measuring points lies 5% above the one of the linear fit. The slope of the linear fit indicates the rate of film thickness reduction  $\psi$ . The measured values of the constant range are averaged and by determining the point of intersection the time of the volume fixation  $t_{EoS}$  can be determined.

The decrease in relative solvent content  $w_l$  was determined by calculating  $w_l$  at every measurement time according to Equation (1) using the measured mass of the wet coating sample  $m_w$  and the mass of the dried coating sample  $m_s$ .

$$w_l(t) = \frac{m_l(t)}{m_l(t) + m_s} = 1 - \frac{m_s}{m_w(t)} \quad (1)$$

For the anode suspension with an initial solvent content of  $w_l = 0.52$  and a drying temperature  $T_{Dr} = 70\text{ }^{\circ}\text{C}$ , the results of the solvent content and the surface temperature are shown in **Figure 2**. A thermocouple was used to measure the coating temperature during the drying of the electrodes. The coating temperature shows lower values in the first seconds until the thermocouple is carefully placed on the coating surface. Since the measuring bead is carefully placed on top of the wet coating, which in this state offers no appreciable resistance, a slight penetration into the coating cannot be completely ruled out. Therefore, in the following the term film temperature  $T_F$  is used instead of surface temperature  $T_s$ . This measuring principle has the advantage over pyrometers as it is independent of changes in the adsorption properties resulting from the change of the coating surface from glossy wet to matt dry. First of all, it is noticeable that the measured temperature remains below the drying temperature of  $T_{Dr} = 70\text{ }^{\circ}\text{C}$  at all times. This can be attributed to the fact that an intermediate temperature of the coating with the ambient air of approx.  $20\text{ }^{\circ}\text{C}$  is reached due to the applied drying method. Furthermore, three sections can be distinguished on the basis of the coating temperature: The first section lasts up to

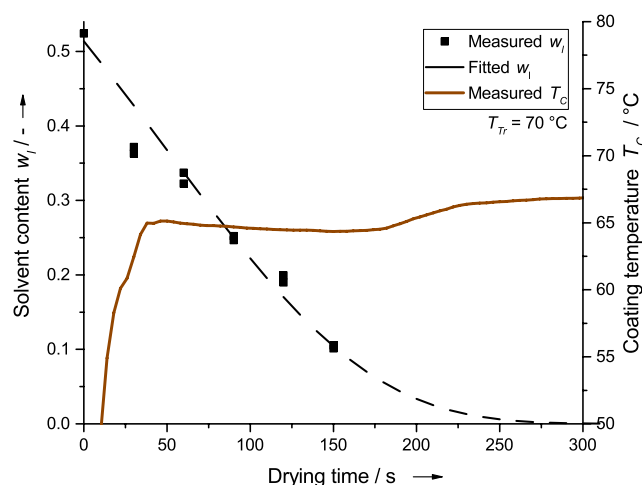


**Figure 2.** Evolution of solvent content  $w_l$  and coating temperature at  $T_{Dr} = 70\text{ }^{\circ}\text{C}$ .

a drying time of around 180 s, in which the coating temperature is approx.  $65\text{ }^{\circ}\text{C}$ . Here, the measured temperature, the steady-state temperature, is lower than the drying temperature due to evaporative cooling. Within the second section until  $\approx 235$ , the temperature increases, which indicates that the amount of evaporating solvent is reduced to such an extent that cooling of the coating surface can no longer maintain the steady-state temperature. Finally, in the third section from 235 s on, a constant temperature of around  $68\text{ }^{\circ}\text{C}$  is reached, which is the dry coating temperature during this drying process. The course of the solvent content can be described as linearly decreasing up to  $t \approx 150$  s. It should be noted that a linear decrease in solvent content is not associated with a constant drying rate, since the change in mass of the solvent is included in both the dividend and divisor, see Equation (1).

The effects of the drying temperature on the drying rate are discussed in Section 2.2. In the range of low solvent contents ( $w_l < 0.1$ ), the adhesive strength of the coating to the substrate has become so strong that a faultless removal of the coating with a spatula was no longer possible and, therefore, sampling in these solvent ranges had to be avoided. For fitting of the spatula samples, a Gumbel fit was chosen, which is linear in the first range and then asymptotically approaches a limit value, in this case, the solvent content  $w_l = 0$ .

In battery cells, intrudable pores of the electrode are filled with electrolytes and thus, significantly contribute to the conductivity of the lithium ions within the coating. The pore structure is formed by drying and reduced to an optimum ratio of ionic to electrical conductivity during the calendaring process step. While porosity is generally referred to as the ratio of the void volume to the total volume of a porous structure, the term for drying is expanded so that porosity also refers to the total volume of pores filled with solvent. During drying, the porosity of the battery electrodes affects mass transfer via the diffusion coefficient in two ways: First, mass transport takes place within the solvent-filled, porous network and influences the diffusion of the binder in the solvent. Furthermore, the porosity with increased drying time and the associated falling liquid level influence the diffusion of the solvent in the gas phase within the coating. To differentiate, the porosity

formed from pores filled with solvent is called  $\varepsilon_{\text{full}}$  and those with solvent-free pores  $\varepsilon_{\text{void}}$ . The total porosity is the sum of these and is used without an index, as shown in Equation 2

$$\varepsilon = \varepsilon_{\text{full}} + \varepsilon_{\text{void}} \quad (2)$$

At the beginning of the drying process, the entire intrudable pore structure is filled with solvent. When the layer thickness decreases during the drying process, this implies a reduction in porosity over the drying time. By directly linking the total porosity with the layer thickness, the development of these two variables is considered in **Figure 3**. The porosities shown here are determined via the layer thickness measured and the solid density and differ slightly from the porosity determined via mercury intrusion due to the method used. From the measured layer thickness and the solvent content over time, an estimation of the layer thickness occupied by the solid components, the solvent-filled pores, and the free pores is shown in **Figure 3** on the left. From this, the decrease of the porosity of filled pores,  $\varepsilon_{\text{full}}$ , and the increase of the percentage of solvent-free pores,  $\varepsilon_{\text{void}}$ , is calculated as depicted in **Figure 3** right. This estimation allows a better understanding of the pore formation over the drying time and provides important information about the degree of pore filling. The assumed layer thickness of the solid, to which the active material and the carbon black belong, results from the material densities and the material proportions. Since no solid is sublimated during drying, the layer thickness that the solids would take up in compressed form without free pores is constant. As in this experiment, the structural changes throughout the drying process are of interest rather than the final microstructural characteristics, the binder is assumed to be completely dissolved in the solvent and is not considered in the solids layer. Directly after coating, solvents and solids take up the entire volume of the coating and accessible pores are filled with solvent. The solvent is removed from the coating during drying, which results in a reduction of the total coating thickness. Since the thickness of the coating, which is taken up by the solvent, is reduced faster, i.e., the drying rate is higher than the rate of reduction of the coating thickness, solvent-free pores are formed even before the volume is fixed at the time of  $t_{\text{EoS}}$ . The porosities

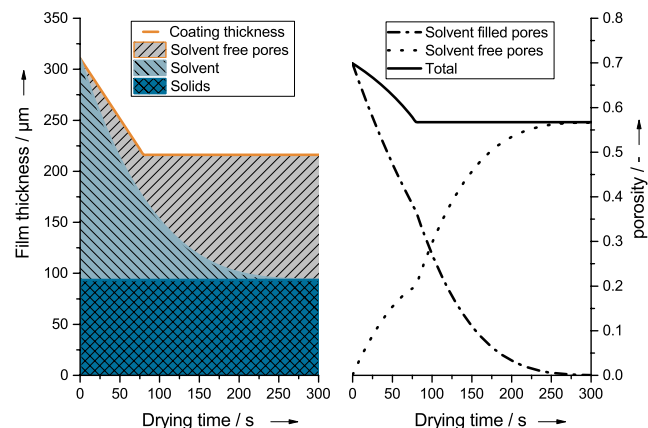


**Figure 3.** Evolution of film thickness over time with respectively the fraction of solvent-free pores, solvent, and solids (left) and the portion of solvent-free and solvent-filled pores in the total porosity (right).

shown in **Figure 3** on the right illustrate the effect of volume fixation on porosity. The total porosity  $\varepsilon$  is reduced with decreasing layer thickness and reaches a constant value at the time  $t_{\text{EoS}}$ . As the solvent-filled porosity  $\varepsilon_{\text{full}}$  decreases, the proportion of solvent-free pores and the associated porosity  $\varepsilon_{\text{void}}$  increases. This must be taken into account during binder migration, as the binder is transported exclusively in the liquid phase. This assumption can be made, among other things, because the melting temperatures of the binders are undercut during drying. Thus, the binder is fixed in solvent-free pores. As a result, the binder in the solvent-free pores is no longer mobile.

## 2.2. Influence of Different Drying Temperatures on Film Properties During Drying

To investigate the influence of the drying temperature  $T_{\text{Dr}}$ , water-based anodes were dried at temperatures of 40 to 80 °C and their layer thickness reduction, coating temperature, and solvent content were determined. Results as shown in **Figure 1** are obtained. Independent of temperature and suspension properties, the electrodes show constant removal rates  $\psi$  during the first drying phase, which is why a single value for the reduction in coating thickness can be used for description. In **Figure 4**, these are displayed together with time  $t_{\text{EoS}}$ , at which the layer thickness is fixed, over  $T_{\text{Dr}}$ . The rate of film thickness decrease  $\psi$  rises exponentially with the drying temperature. In the considered temperature range of  $T_{\text{Dr}} = 40\text{--}80$  °C, the rate of film thickness decrease  $\psi$  goes up from  $\psi$  ( $T_{\text{Dr}} = 40$  °C) =  $0.16 \mu\text{m s}^{-1}$  to  $\psi$  ( $T_{\text{Dr}} = 80$  °C) =  $2.5 \mu\text{m s}^{-1}$ . The time in which the reduction of the film thickness takes place decreases in the same measure. Consequently,  $t_{\text{EoS}}$  and  $\psi$  are inversely proportional to each other. With increased temperature  $T_{\text{Dr}}$ , the time in which the film formation takes place decreases, and the rate  $\psi$  increases to the same extent, so that the resulting coating thickness is almost constant. The result of this relationship is that, regardless of the drying temperature, the electrodes have nearly the same final coating thickness  $\delta_{\text{B, fixed}}$  within the scope of deviations caused by the measurement. This results in Equation (2), independent of the drying temperature

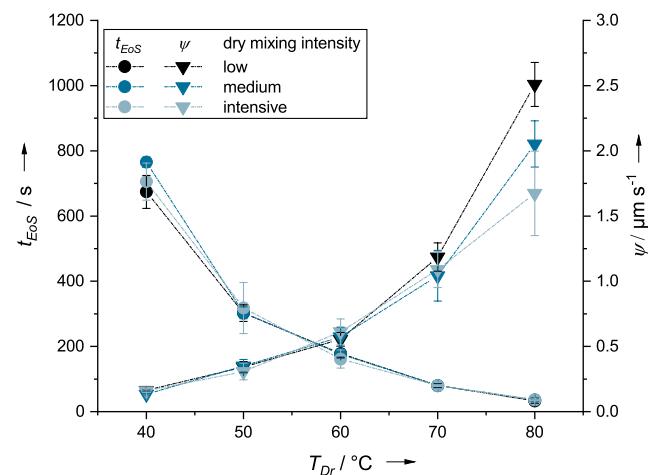


**Figure 4.** End of shrinkage  $t_{\text{EoS}}$  and shrinkage rate  $\psi$  for different drying temperatures and mixing intensities.

$$\delta_{B,\text{fixed}} = \delta_{B,\text{Start}} - \psi t_{\text{EoS}} \quad (3)$$

In addition to the series of tests at different temperatures, results of a variation of the mixing procedure were added in this diagram, whereby the active material and the carbon black were separately dry premixed in a high-intensity mixer, followed by the mixing procedure that was also used for the basic variant. As Figure 4 shows, as the intensity of dry mixing increases, the rate of decrease in film thickness decreases, but not the time of decrease.

The mass loading of the high-intensity mixed electrodes is  $\approx 22 \text{ mg cm}^{-2}$ , which is slightly higher than the base variant with  $20.1 \text{ mg cm}^{-2}$ . Since, however, no change in the absolute removal rate can be observed with increasing wet film thickness, respectively, with increasing area weight of the dry electrode, which is further discussed in Figure S1, Supporting Information, it can be concluded for the variation of the carbon black decomposition that a higher mixing intensity of active material and carbon black is accompanied by a reduction of the removal rate due to the already in the wet state more compact electrode structure.

For the anodes dried at different temperatures, the solvent content  $w_l$  was determined by scraping off the coating during drying with subsequent heating and weighing, and the area-related solvent mass reduction rate  $\dot{m}_l$  was calculated from this, as shown in Figure 5. This illustration demonstrates the differentiation between the decrease in relative solvent content and the mass reduction rate already described in the previous section: A linear, negative gradient of the solvent content  $w_l$  is not associated with a constant mass reduction rate  $\dot{m}_l$ . Although this can be assumed at low drying temperatures, since the decrease is so small that a quasi-constant rate can be monitored, with increasing  $T_{\text{Dr}}$  and, as expected, increasing drying rate, a constant drying rate is less and less achieved. Thus, at  $T_{\text{Dr}} = 80^\circ\text{C}$  an instant decrease of  $\dot{m}_l$  can be observed. Overall, it should be noted that the drying rates achieved here remain significantly below those

achieved on a production scale with residence times in the dryer of approx. 1 min. This is due to the conductive, discontinuous drying method and is assessed as acceptable for these fundamental investigations.

In Figure 6, the measured coating temperatures  $T_C$  as a function of  $T_{\text{Dr}}$  are shown. First of all, it is noticeable that the measured coating temperatures deviate more and more from the set temperatures the higher they become. While at  $T_{\text{Dr}} = 40^\circ\text{C}$  no significant difference between the set and actual temperatures can be determined, at  $T_{\text{Dr}} = 80^\circ\text{C}$  the coating temperature is clearly below  $80^\circ\text{C}$  even at the end of drying. This can be attributed to the fact that in this model design with conductive drying the environment is at room temperature. Although the target temperatures are reached by the heating plate, a temperature gradient is established within the layer due to the cooler

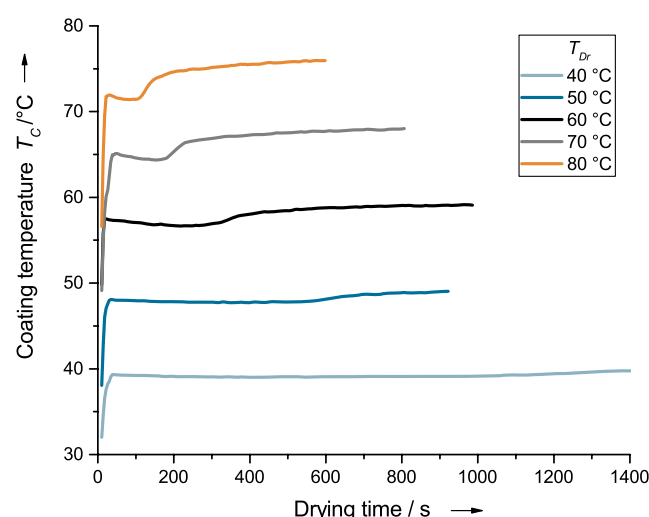


**Figure 6.** Evolution of coating temperature  $T_C$  over time.

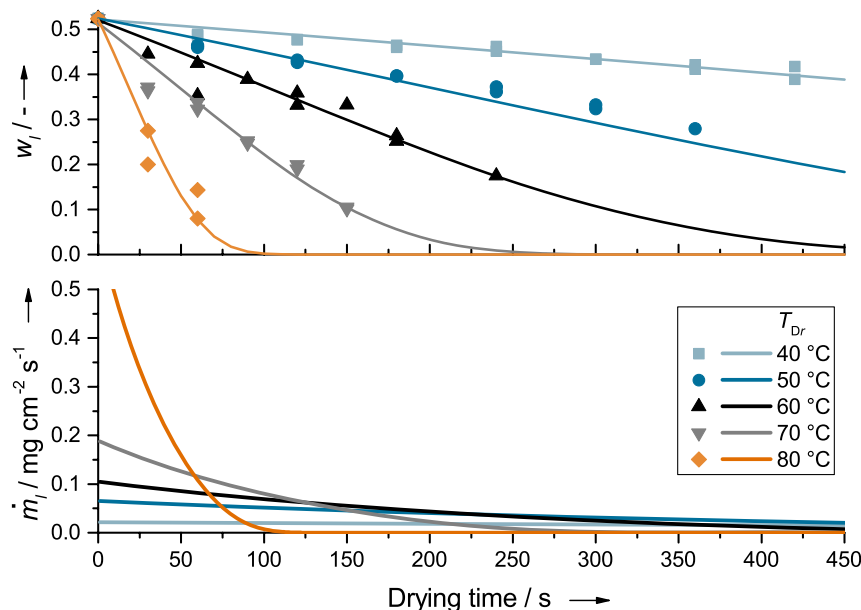


**Figure 5.** Solvent content (top) and area-related solvent mass reduction rate (bottom) over time for different drying temperatures.



temperatures above the heating plate. The further  $T_{Dr}$  deviates from the ambient temperature, the less the target value is reached in the coating. Furthermore, it can be seen in which time period a reduction of coating temperature  $T_C$  is present due to the evaporative cooling of the water. This becomes particularly clear at the high temperatures of 70 and 80 °C, where high drying rates lead to a strongly pronounced cooling effect. As a result of the high drying rates, the increase of the temperature in the second drying stage is shifted to even shorter drying times.

### 2.3. Influence of Different Drying Temperature on Final Electrode Properties

The amount of binder in the battery electrode as an electrochemically inactive component should be kept as low as possible, while ensuring sufficient cohesion within the coating and adhesion to the substrate film. This can only be achieved if the binder is present where it is needed, i.e., homogeneously inside the coating and at the interface to the substrate film. This results in the necessity of a homogeneous distribution of the binder over the layer thickness or, ideally, a gradient with increasing binder content towards the substrate. The binder migration can be analyzed by energy dissipative X-ray spectroscopy (EDX) and adhesion tests.<sup>[3]</sup> Figure 7 shows the normalized amount of Na and points it out by the use of a linear regression. In addition, the adhesive strength is shown in Figure 8. If the binder is distributed homogeneously, the normalized binder distribution over the four coating segments would be constant at 25%. A uniform distribution is most likely to be present at 40–60 °C, which is also consistent with the adhesion tests in Figure 8, since the highest adhesive strengths were achieved at these drying temperatures. The uneven binder distribution is the strongest at  $T_{Dr} = 80$  °C with the lowest adhesive strength of  $\sigma_z \approx 880$  kPa. The inhomogeneous binder distribution at  $T_{Dr} = 40$  °C is remarkable in so far as the electrode has the lowest drying rates, see Figure 5, which is usually considered the most decisive parameter of binder migration during drying. Due to the low temperature,

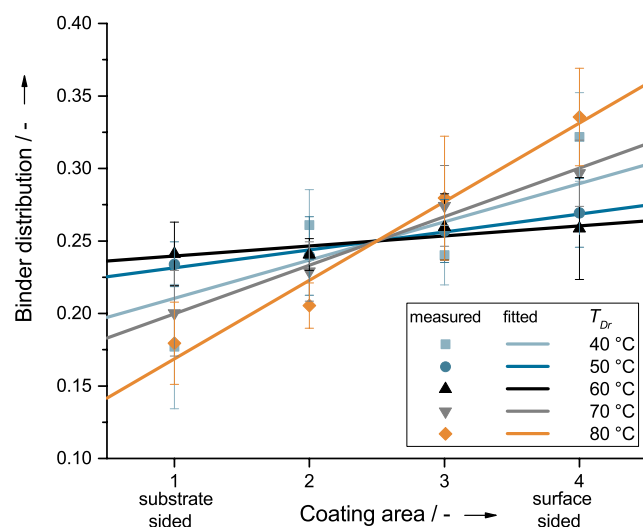


**Figure 7.** Distribution of binder in the electrodes dried at different temperatures.

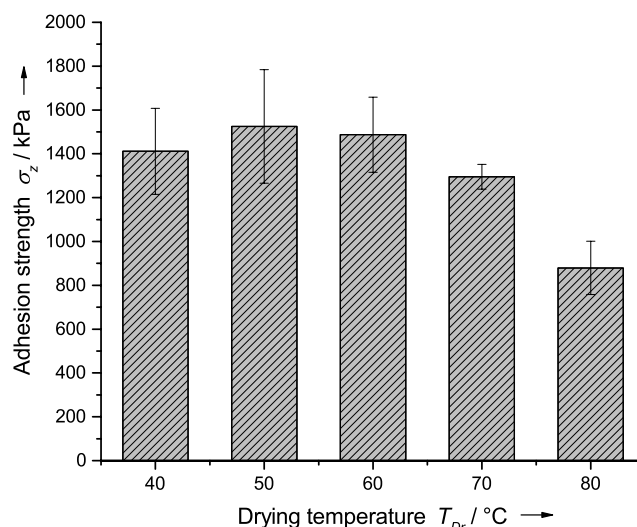


**Figure 8.** Adhesion strength of electrodes dried at different temperatures.

however, the diffusively acting forces are less pronounced than at higher drying temperatures, based on the reduced particle motion and higher viscosity. Overall, the two methods show a similar trend in that the strongest binder migration is detected at a drying temperature  $T_{Dr} = 80$  °C and a more homogeneous binder distribution is achieved with decreasing temperature and, thus, lower evaporation rates. Furthermore, the degree of binder migration increases with the increasing rate of layer shrinkage  $\psi$  of the coating. An exception to this process is the anode dried at  $T_{Dr} = 40$  °C. Due to the low temperatures and thus higher viscosity, the diffusion of the binder could be inhibited so that a compensation of the convective flow is not possible. For the variation of the mixing procedure, the decrease rate behaves correspondingly also the adhesion strength, so at the highest mixing intensity and the lowest temperature also the highest adhesion strength can be measured. The results are shown in Figure S2, Supporting Information.

The mercury intrusion allows a differentiated characterization of the pore structure by means of the pore diameter distribution as shown in Figure 9. The pore diameter distribution of the active material is characterized by pores in the  $\mu\text{m}$  range, which is determined by a median particle size value of  $x_{50} = 19 \mu\text{m}$  and a flake-like particle shape. With a primary particle size of  $x_{50} = 40 \text{ nm}$  and an aggregated and agglomerated secondary structure, the pores inherent in carbon black are in the nm range. As the binder adheres to the surfaces of the active material and the carbon black in electrodes and forms binder bridges, it does not form pores on its own and, therefore, can be neglected in this analysis. The active material and carbon black are mixed in electrodes, whereby the carbon black agglomerates have been partially broken down during the dispersion process.<sup>[2,5–7]</sup> Furthermore, carbon black agglomerates settle in the spaces between the active material, as a result of which the pore diameter distribution in electrodes appears as shown in Figure 9. The pore structure of the anodes investigated here is significantly influenced by the pores of the active material with a maximum of  $3.7 \mu\text{m}$ . The carbon black-inherent pores are assigned to the pore range  $0.1\text{--}1.0 \mu\text{m}$ . The pore size distributions of the anodes

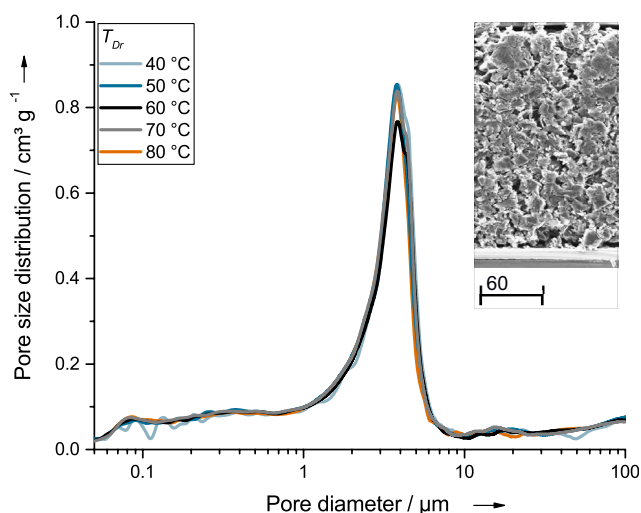


**Figure 9.** Pore size distribution for electrodes dried at different temperatures and exemplary secondary electron microscope (SEM) image of the anode dried at 40 °C.

dried at different temperatures can be considered identical. This is in accordance with a constant coating thickness at varying drying temperatures. The SEM image embedded in diagram 9 is exemplary for the electrodes discussed here and shows a cross-section of them. As is typical for electrodes, the cross-section shows active material and carbon black agglomerates traversed by the pores just discussed. In terms of purely visual assessment, no differences between the electrodes are discernible. In conclusion, a change in the drying temperature and the resulting binder distribution within the coating does not cause differences in the pore structure as it can be measured by mercury intrusion. This underlines the assumption that no pores associated with the binder are formed.

### 3. Conclusions

This study aims at elucidating the dependencies of the electrode properties on the drying temperature. Therefore, the drying of battery water-based anodes at different temperatures was investigated using a model setup in which the layers were dried conductively. The rate of solvent removal and the time until the layer is fixed,  $t_{\text{EoS}}$ , were found to be the decisive parameters for describing the experiments.

Thus, an increase in drying temperature causes the layer shrinkage rate to increase exponentially and  $t_{\text{EoS}}$  to decrease to the same extent. The mixing procedure was also identified as a further influencing factor, with high-intensity mixing being associated with a reduced reduction rate. The differences in drying rate and drying time lead to different binder distributions within the electrode. Due to fast evaporation, the binder accumulates at the electrode surface whereas for lower evaporation rates diffusion counteracts this effect resulting in a more evenly distributed binder. Reducing the temperature and, therefore, the drying rate even further down to 40 °C causes viscosity and with that diffusion to decrease to an extent that hinders the binder to distribute uniformly. In contrast to the binder, the pore structure

of the electrodes and the coating height do not change. This leads to the assumption, that the formation of pores proceeds independently of the binder. Overall it can be assumed that the distribution of the binder and, therefore, the mechanical integrity of the electrode can be controlled to a large extent by tuning the evaporation rate and the drying temperature. With this knowledge, large-scale drying processes can be tailored to produce porous, yet mechanically stable electrodes by adjusting the drying rate and the temperature which act as counteracting forces influencing in terms of distributing the binder. To investigate the influencing factors regarding the formation of the structure and the interaction with the binder more thoroughly, the numerical simulation could be part of future work, building up on the presented findings, to enable fast and resource-saving process development.

### 4. Experimental Section

**Slurry Preparation:** For the preparation of anodes synthetic, surface-modified graphite was used as active material. The particle median size is  $x_{50} = 19 \mu\text{m}$  with a specific surface area of  $3 \text{ m}^2 \text{ g}^{-1}$ . Furthermore, the theoretical specific discharge capacity was  $362 \text{ mA h g}^{-1}$ . As a conductive agent, carbon black (C-Nergy Super C65, Imerys) with a specific surface of  $63 \text{ m}^2 \text{ g}^{-1}$  and a primary particle size of  $x_{50} = 40 \text{ nm}$  was added. Na-CMC (Walogel CRT 2000 PA, Dow Wolff) and SBR (Lipaton SB 5521, Synthomer) were added as binders. The recipe formulation of the solids was 90 wt% active material, 5 wt% carbon black, 2.5 wt% CMC binder, and 2.5 wt% SBR binder. With this robust formulation, process variation outside the optimal drying window is possible and characterizable electrodes can be produced.

For the preparation of the slurry in a batch-wise manner, first, the solid components were dry mixed in a shaker mixer (Turbula T2F, Willi A. Bachofen) for 15 min before the solids were dispersed in the solvent (deionized water) by means of a dissolver (Dispermat C A60, VMA-Getzmann) for 60 min at 15 °C with a tip speed of  $9 \text{ m s}^{-1}$  and a 20 min degassing step, resulting in a solids content in the slurry of 48 wt%.

For the variation of the mixing procedure, the active material and carbon black were dry premixed for 2 min. This was carried out in the Nobilta high-intensity mixer from Hosokawa Alpine. An annular gap of 3 mm between the rotor blades and the casing wall leads to a breakdown of the carbon black agglomerates. The speeds used are 1500 and  $2000 \text{ s}^{-1}$ , respectively. After the high-intensity mixing, the slurry preparation was carried out according to the basic slurry.

**Coating and Drying:** The prepared slurry was coated on the substrate (copper foil with a thickness of  $10 \mu\text{m}$ ) with a discontinuous automated coating device (ZAA 2300, Zehntner) by knife coating. A coating width of 80 mm and a coating speed of  $10 \text{ mm s}^{-1}$  were set. Conductive heating was applied via a heating plate able to produce temperatures up to 160 °C. To overcome the issue of an overlap of the heating-up with the first drying phase, the slurry and the substrate were preheated to the desired drying temperature ( $T = 40, 50, 60, 70$ , and  $80 \text{ }^\circ\text{C}$ ).

During drying, the decrease in film thickness was analyzed by non-contact coating thickness sensors (LK-H052, Keyence) via laser triangulation with a sampling rate of  $5 \text{ s}^{-1}$ . To eliminate measuring errors, the height of the coating film as well as the position of the substrate was measured so that the difference of the positions delivers the fluctuation-adjusted coating film thickness. The whole measuring setup was preheated to a constant temperature to account for the temperature sensitivity of the setup. The measurements were repeated four times.

The temperature determination in the model experiments was carried out using a single-wire thermocouple of type K with a free welded tip at a conductor size of 0.076 mm using the OM-USB-TC-AI data logger from OMEGA Engineering. Due to the small size of the thermocouple, it is possible to measure the temperature of the coating surface. However, a slight penetration

into the coating cannot be completely excluded, so in the following, the determined temperature is referred to as the coating temperature  $T_C$ .

To determine the solvent content during the drying process, the coated film was scraped off with a spatula at specified times and weighed, before the contained solvent was removed via heating and the sample was weighed again.

**Characterization of Electrodes:** Using an SEM (EVO LS25, Carl Zeiss NTS) with integrated EDX (Q455 CFlash 5030/300, Bruker AXS) the binder distribution over the coating cross section was measured directly. During the analysis of the binder distribution, elements of the binders that are not present in the remaining solid components are evaluated. Therefore, the sodium distribution is analyzed for water-based anodes. To be able to analyze the binder distribution in the electrodes, a cross-section of these is made and the coating height was divided into four sections. The magnification was adapted to the coating height in each case. Despite the advantage of a direct measurement of the binder, this method has the disadvantage of a small sample quantity. To counteract this, five measuring points were analyzed in each of the four sections.

The adhesive strength of the electrode coating was measured with a material testing machine (Z020, Zwick) with 68 N and a pulling speed of  $100 \text{ mm min}^{-1}$  according to Haselrieder et al.<sup>[32]</sup> Statistical significance was ensured by measuring 10 samples.

To analyze the electrode structure, the pore size distributions of the dried electrodes were obtained by mercury intrusion (Poremaster 60 GT, Quantachrome), as described by Froböse et al.<sup>[33]</sup> Samples with an area of  $20 \text{ cm}^2$  were measured in a pressure range between 7 kPa and 207 MPa to investigate the volume of pores ranging from 1 nm to 200  $\mu\text{m}$ .

## Supporting Information

Supporting Information is available from the Wiley Online Library or from the author.

## Acknowledgements

The authors would like to thank the Nds. Ministerium für Wissenschaft und Kultur of the State of Lower Saxony for the financial support of this work with Graduiertenkolleg Energiespeicher und Elektromobilität Niedersachsen (GEENI). Furthermore, this work has received funding from the European Union's Horizon 2020 research and innovation programme under grant agreement No 875247.

Open Access funding enabled and organized by Projekt DEAL.

## Conflict of Interest

The authors declare no conflict of interest.

## Data Availability Statement

The data that support the findings of this study are available from the corresponding author upon reasonable request.

## Keywords

binders, drying, electrodes, lithium-ion batteries, microstructures

Received: June 28, 2022

Revised: October 7, 2022

Published online:

- [1] A. Kwade, W. Haselrieder, R. Leithoff, A. Modlinger, F. Dietrich, K. Droeder, *Nat. Energy* **2018**, 3, 290.
- [2] H. Bockholt, M. Indrikova, A. Netz, F. Golks, A. Kwade, *J. Power Sources* **2016**, 325, 140.
- [3] W. Haselrieder, S. Ivanov, H. Y. Tran, S. Theil, L. Froböse, B. Westphal, M. Wohlfahrt-Mehrens, A. Kwade, *Prog. Solid State Chem.* **2014**, 42, 157.
- [4] G. Lenze, H. Bockholt, C. Schilcher, L. Froböse, D. Jansen, U. Krewer, A. Kwade, *J. Electrochem. Soc.* **2018**, 165, 314.
- [5] W. B. Hawley, J. Li, *J. Energy Storage* **2019**, 25, 100862.
- [6] W. Bauer, D. Nötzel, V. Wenzel, H. Nirschl, *J. Power Sources* **2015**, 288, 359.
- [7] H. Bockholt, W. Haselrieder, A. Kwade, *Powder Technol.* **2016**, 297, 266.
- [8] J. K. Mayer, L. Almar, E. Asylbekov, W. Haselrieder, A. Kwade, A. Weber, H. Nirschl, *Energy Technol.* **2020**, 8, 1900161.
- [9] M. Wang, D. Dang, A. Meyer, R. Arsenaault, Y.-T. Cheng, *J. Electrochem. Soc.* **2020**, 167, 100518.
- [10] M. Schmitt, M. Baunach, L. Wengeler, K. Peters, P. Junges, P. Scharfer, W. Schabel, *Chem. Eng. Process.* **2013**, 68, 32.
- [11] R. Diehm, M. Müller, D. Burger, J. Kumberg, S. Spiegel, W. Bauer, P. Scharfer, W. Schabel, *Energy Technol.* **2020**, 8, 2000259.
- [12] M. Baunach, S. Jaiser, S. Schmelzle, H. Nirschl, P. Scharfer, W. Schabel, *Drying Technol.* **2016**, 34, 462.
- [13] S. Jaiser, A. Friske, M. Baunach, P. Scharfer, W. Schabel, *Drying Technol.* **2017**, 35, 1266.
- [14] S. Jaiser, M. Müller, M. Baunach, W. Bauer, P. Scharfer, W. Schabel, *J. Power Sources* **2016**, 318, 210.
- [15] B. Westphal, H. Bockholt, T. Gunther, W. Haselrieder, A. Kwade, *ECS Trans.* **2015**, 64, 57.
- [16] B. G. Westphal, A. Kwade, *J. Energy Storage* **2018**, 18, 509.
- [17] M. Stein IV, A. Mistry, P. P. Mukherjee, *J. Electrochem. Soc.* **2017**, 164, A1616.
- [18] G. Lenze, F. Röder, H. Bockholt, W. Haselrieder, A. Kwade, U. Krewer, *J. Electrochem. Soc.* **2017**, 164, A1223.
- [19] T. Günther, D. Schreiner, A. Metkar, C. Meyer, A. Kwade, G. Reinhart, *Energy Technol.* **2020**, 8, 1900026.
- [20] C. Meyer, H. Bockholt, W. Haselrieder, A. Kwade, *J. Mater. Process. Technol.* **2017**, 249, 172.
- [21] C. Sangrós Giménez, B. Finke, C. Schilde, L. Froböse, A. Kwade, *Powder Technol.* **2019**, 349, 1.
- [22] H. Hagiwara, W. J. Suszynski, L. F. Francis, *J. Coat. Technol. Res.* **2014**, 11, 11.
- [23] S. Jaiser, J. Kumberg, J. Klaver, J. L. Urai, W. Schabel, J. Schmatz, P. Scharfer, *J. Power Sources* **2017**, 345, 97.
- [24] S. Jaiser, L. Funk, M. Baunach, P. Scharfer, W. Schabel, *J. Colloid Interface Sci.* **2017**, 494, 22.
- [25] Z. Liu, P. P. Mukherjee, *J. Electrochem. Soc.* **2014**, 161, E3248.
- [26] Z. Liu, V. Battaglia, P. P. Mukherjee, *Langmuir* **2014**, 30, 15102.
- [27] Z. Liu, D. L. Wood, P. P. Mukherjee, *Phys. Chem. Chem. Phys.* **2017**, 19, 10051.
- [28] M. M. Forouzan, C.-W. Chao, D. Bustamante, B. A. Mazzeo, D. R. Wheeler, *J. Power Sources* **2016**, 312, 172.
- [29] A. C. Ngandjong, A. Rucci, M. Maiza, G. Shukla, J. Vazquez-Arenas, A. A. Franco, *J. Phys. Chem. Lett.* **2017**, 8, 5966.
- [30] A. Rucci, A. C. Ngandjong, E. N. Primo, M. Maiza, A. A. Franco, *Electrochim. Acta* **2019**, 312, 168.
- [31] F. Font, B. Protas, G. Richardson, J. M. Foster, *J. Power Sources* **2018**, 393, 177.
- [32] W. Haselrieder, B. Westphal, H. Bockholt, A. Diener, S. Höft, A. Kwade, *Int. J. Adhes. Adhes.* **2015**, 60, 1.
- [33] L. Froboese, P. Titscher, B. Westphal, W. Haselrieder, A. Kwade, *Mater. Charact.* **2017**, 133, 102.